Monthly Notices
of the
ROYAL ASTRONOMICAL SOCIETY

MNRAS **441,** 2996–3008 (2014) doi:10.1093/mnras/stu774

A hyperspectral view of Cassiopeia A

Alexandre Alarie,[1,2★] Antoine Bilodeau[1,2] and Laurent Drissen[1,2]

[1] *Département de physique, de génie physique et d'optique, Université Laval, Québec, QC G1V 0A6, Canada*
[2] *Centre de Recherche en Astrophysique du Québec, Canada*

Accepted 2014 April 16. Received 2014 April 16; in original form 2013 July 12

ABSTRACT

We used the imaging Fourier transform spectrometer Spectromètre Imageur de l'Observatoire du Mont-Mégantic (SpIOMM) to obtain hyperspectral cubes of the young supernova remnant Cassiopeia A (Cas A). The cubes contain over 5000 spatially resolved spectra covering the spectral range 6480–7050 Å. We first investigate the slow-moving N-rich quasi-stationary flocculi by measuring their radial velocity as well as the [N II] λ6583/Hα ratio. No correlation between their radial velocity and [N II] λ6583/Hα ratio with their location has been found. We used multi-epoch observations from the *Hubble Space Telescope* to create a proper motion map, showing the displacement of several filaments over the most part of Cas A. Combining data from SpIOMM and *Hubble*, we re-evaluate the distance to Cas A and obtained 3.33 ± 0.10 kpc, which is in good agreement with previous estimates. Finally, we obtain a three-dimensional spatial view of the [S II] λλ6716, 6731 emissions showing their location, expansion velocity and the [S II] doublet line ratio for multiple locations in the remnant. The velocity asymmetry reported by previous analyses is clearly visible. Also, the [S II] doublet ratio (with a mean value of 0.5 ± 0.2) indicates a very high and variable electronic density throughout the remnant.

Key words: techniques: imaging spectroscopy – proper motions – ISM: individual objects: Cassiopeia A – ISM: supernova remnants.

1 INTRODUCTION

Cassiopeia A (Cas A) is one of the most studied supernova remnants (SNR) due to its relative proximity to earth ($3.4\,^{+0.3}_{-0.1}$ kpc; Reed et al. 1995) and its young age with an estimated explosion date of around AD 1680 (Thorstensen, Fesen & van den Bergh 2001; Fesen et al. 2006b), making it one of the best targets for studying SNR evolution. The optical spectrum from the SN explosion near maximum brightness has been observed from scattered light echoes of the SN outburst (Rest et al. 2008, 2011; Besel & Krause 2012) and indicated that Cas A was probably a Type IIb SN from a star of initial mass 15–25 M$_{\odot}$, which might have lost much of its hydrogen envelope due to binary interaction (Young et al. 2006; Krause et al. 2008).

Cas A has been observed extensively in the radio, infrared, optical and X-ray, all emanating from different regions in the remnant. The blast wave drives an outgoing forward shock expanding through the circumstellar medium that can be seen as faint X-ray filaments outside a main shell (Gotthelf et al. 2001; Laming & Hwang 2003). The interaction with the circumstellar material and the interstellar medium (ISM) results in a reverse shock that is driven back into the outgoing ejecta. The ejecta is then shocked, heated and collisionally ionized forming a 'bright ring' of shock-heated SN debris consisting of undiluted ejecta rich in O, Si, S, Ar, Ca and Fe (Chevalier & Kirshner 1978; Douvion, Lagage & Cesarsky 1999; Hughes et al. 2000; Willingale et al. 2002; Hwang & Laming 2003; Ennis et al. 2006). Very high velocity debris exhibiting strong O, S and Ar lines, known as fast-moving knots (FMKs), along with mixed emission knots (MEKs) which show both strong N and S lines have been detected and carefully catalogued (Fesen 2001; Fesen et al. 2006a,b, 2011; Hammell & Fesen 2008). These debris can be found in a 'flare' or 'jet' along the north-east and south-west limb from the remnant centre. The presence of such a jet and its counter-jet is thought to be the evidence that Cas A's progenitor exploded in a highly aspherical fashion.

Apart from the material ejected by the SN, slow-moving N-rich clumps ('quasi-stationary flocculi', hereafter QSFs) showing both Balmer emission and strong [N II] λλ6548, 6583 lines were identified (van den Bergh 1971; Chevalier & Kirshner 1978; van den Bergh & Kamper 1985; Hurford & Fesen 1996). These QSFs are consistent with CNO-processed, circumstellar mass-loss material prior the explosion, indicating that Cas A's progenitor had an N-rich photosphere at the time of the outburst with still some hydrogen left.

Since Cas A is relatively young, many parts in the remnant exhibit high Doppler shifts. Therefore, several Doppler reconstructions of Cas A's main shell ejecta have been conducted using optical, infrared and X-ray data. The first Doppler reconstructions have been obtained by Lawrence et al. (1995) and Reed et al. (1995) using the

★ E-mail: alexandre.alarie.1@ulaval.ca

O and S lines from optical observations. Both reported asymmetry in the ejecta velocity and demonstrated that the FMKs are distributed into ring-like structures. DeLaney et al. (2010) created an impressive 3D view of Cas A using both infrared and X-ray Doppler velocity measurement from the *Spitzer Space Telescope* and *Chandra X-ray Observatory* following an extensive reconstruction. Their study confirmed the presence of large ring-like structures, multiple ejecta jets/pistons and a tilted thick disc. 3D maps of the material in the centre of the remnant have also been obtained recently using *Spitzer* observations (Isensee et al. 2010, 2012), where the material has not yet interacted with the reverse shock. IR 3D maps of Cas A unveil major asymmetries both on global scale (DeLaney et al. 2010) and smaller scale (Isensee et al. 2010, 2012) of ejecta throughout the entire remnant. Very recently, a new 3D view of Cas A in optical was obtained by Milisavljevic & Fesen (2013) using a technique similar to that of DeLaney et al. (2010). Their analysis reveals similar geometry and velocity asymmetry as reported by previous studies, and clearly illustrates the relative position of the outer ejecta knots compared to the main shell.

Such reconstructions require a large investment, both in observation time and workforce, to retrieve all the data needed. Most of the time, such projects must be extended through many years, limiting what can be done in a given period of time. In this paper, we present optical observations obtained with the imaging Fourier transform spectrometer Spectromètre Imageur de l'Observatoire du Mont-Mégantic (SpIOMM) and archived *Hubble Space Telescope* (*HST*) data. After a description of the instrument and observations in Section 2, we begin by re-investigating the slower moving N-rich clumps QSF of circumstellar material in Section 3.1. In Section 3.2, we present a proper motion map showing the relative displacements of several filaments using *Hubble* observations. We then explain the deconvolution used in Section 3.3 in order to create a 3D velocity map of Cas A. From this map, we then independently estimate the distance to Cas A (Section 3.4). Finally, we use the proper motion and 3D velocity maps to create a full 3D spatial view of Cas A presented in Section 3.5 and discuss the [S II] λλ6716, 6731 ratio in Section 3.6.

2 OBSERVATIONS

2.1 SpIOMM observations and data reduction

Hyperspectral cubes of Cas A were obtained with the wide-field imaging Fourier transform spectrometer SpIOMM (Bernier et al. 2008; Drissen et al. 2008, 2012) during the nights of 2009 September 17–18 and 2011 December 3–4 using the Ritchey–Chrétien 1.6 m telescope of the Observatoire du Mont-Mégantic (OMM).

SpIOMM, which is essentially a Michelson interferometer combined with imaging optics and two detectors, can acquire the spectrum of every source of light in a 12 arcmin field of view, in selected bandpasses of the visible range (3500–8500 Å). Thousands of spatially resolved spectra can therefore be obtained of an extended object in a single sequence of observation. The spectral resolution can be set by the observer between $R = 1$ and 25 000 while the spatial resolution is limited by the seeing (typically 2 arcsec). The best balance between spectral resolution, spectral coverage and signal-to-noise ratio is adjusted according to the science objectives and surface brightness of the source. At the time of the observations, only one of the two interferometer's output ports was used, equipped with a 1340 × 1300–0.55 arcsec pixel Princeton Instrument CCD. The images were binned (2 × 2) online, resulting in 435 000–1.1 arcsec pixels. The data are stored in a form of hyperspectral cubes with two spatial and one spectral dimensions (see Fig. 1)

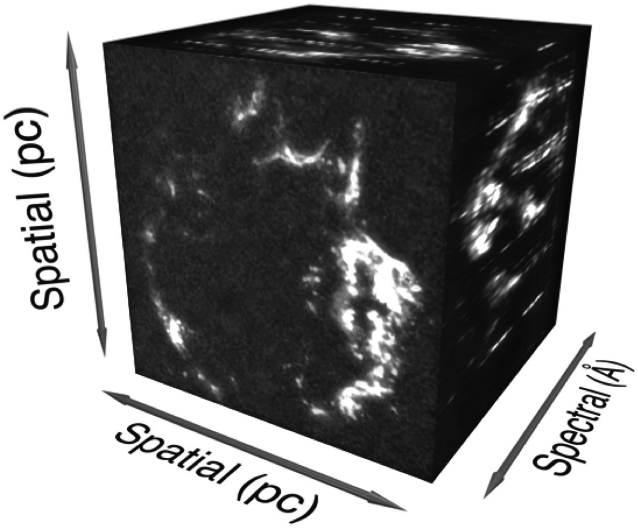

Figure 1. A 3D view of an ~5 arcmin × 5 arcmin section of the second red hyperspectral cube. The front shows the collapsed image of Cas A as viewed by SpIOMM (east is to the top, north to the right), while the third dimension corresponds to the spectral axis, in this case the projection of all the spectra on the side.

Despite the fact that the instrument is capable of observing the entire visible band in a single data cube, it is necessary to use interference filters to acquire the desired data with a decent spectral resolution in a reasonable amount of time. We therefore obtained two hyperspectral cubes with interference filters. For the first observation, we used a red filter (λλ6480–6820 Å) to limit the bandwidth to the [N II] λλ6548, 6583, Hα λ6563 and [S II] λλ6716, 6731 emission lines. We measured the full width at half-maximum (FWHM) of the Hα line from the extended diffuse interstellar component across the field to be 2.5 Å, corresponding to an instrumental resolution $R \sim 2600$ at 6563 Å. Although the selected red filter can encompass the vast majority of the filaments in Cas A, some were reported receding from us at high velocities, therefore potentially being shifted outside the filter bandpass. To ensure the detection of all of the [S II]-rich filaments, another red filter was used with a spectral coverage of 6450–7050 Å and a similar spectral resolution, $R \sim 2500$. The observational parameters are summarized in Table 1.

The first steps in the data reduction for a hyperspectral cube are identical to those of normal CCD imaging: bias and dark subtraction as well as flat-field corrections for every image. All frames were co-registered to correct guiding and minor flexure errors during observation (resulting in a slow drift of ~3 arcsec during the entire acquisition). After applying all the corrections, each pixel was then Fourier transformed and spectrally calibrated using a high-resolution data cube of a reference HeNe laser at 632.8 nm. A more

Table 1. Characteristics of the hyperspectral cubes.

Characteristics	Red filter #1	Red filter #2
Spectral range (Å)	6480–6780	6600–6950
Spectral resolution (Å)	2.5	2.7
Exposure time per image (s)	30	30
Number of images	325	438
Total observing time (min)	185	272

Table 2. List of Hubble Legacy Archive data sets chosen to create multi-epoch optical maps of Cas A.

Data set name	Year	Filter	Exposure time (s)
hst_08281_01_wfpc2_f450w_wf	2000	*F450W*	4 × 700
hst_08281_01_wfpc2_f675w_wf	2000	*F675W*	8 × 500
hst_08281_02_wfpc2_f450w_wf	2000	*F450W*	4 × 700
hst_08281_02_wfpc2_f675w_wf	2000	*F675W*	8 × 500
hst_08281_03_wfpc2_f450w_wf	2000	*F450W*	4 × 700
hst_08281_03_wfpc2_f675w_wf	2000	*F675W*	8 × 500
hst_09238_01_wfpc2_f450w_wf	2002	*F450W*	4 × 700
hst_09238_01_wfpc2_f675w_wf	2002	*F675W*	4 × 500, 4 × 400
hst_09238_02_wfpc2_f450w_wf	2002	*F450W*	4 × 700
hst_09238_02_wfpc2_f675w_wf	2002	*F675W*	8 × 500
hst_09238_03_wfpc2_f450w_wf	2002	*F450W*	4 × 700
hst_09238_03_wfpc2_f675w_wf	2002	*F675W*	4 × 500
hst_11337_01_wfpc2_f450w_wf	2008	*F450W*	4 × 600
hst_11337_01_wfpc2_f675w_wf	2008	*F675W*	4 × 600
hst_11337_02_wfpc2_f450w_wf	2008	*F450W*	4 × 600
hst_11337_02_wfpc2_f675w_wf	2008	*F675W*	4 × 600
hst_11337_03_wfpc2_f450w_wf	2008	*F450W*	4 × 600
hst_11337_03_wfpc2_f675w_wf	2008	*F675W*	4 × 600

detailed description of the data reduction process is presented in Martin, Drissen & Joncas (2012). A final calibration sanity check was provided by the rest-frame night-sky emission lines of OH (at 649.87, 653.30, 655.36 nm), present across the entire field of view.

2.2 *HST* archives

In order to map the proper motion of the remnant's ejecta knots (Section 3.2), high spatial resolution observations at multiple epochs were required. Twenty data sets containing optical observations of Cas A obtained using the Wide Field Planetary Camera 2 (WFPC2) were chosen from the *HST* archives. Table 2 lists the selected data sets. The WFPC2 images were acquired with the broad-band *F675W* and *F450W* filters. The *F675W* and *F450W* images were taken in 2000, 2002 and 2008. All 2000 and 2002 observations were requested by R. A. Fesen, while all 2008 observations were requested by D. J. Patnaude. A detailed description and analysis of these observations can be found in Fesen et al. (2001, 2011) and Morse et al. (2004).

Observations taken with other filters were available but did not span as many years. With a bandpass of 6000–7600 Å, the *F675W* filter encompasses the [S II] λλ6716, 6731, [O II] λλ7319, 7330, [O I] λλ6300, 6364, [N II] λλ6548, 6583, Hα λ6563 and [Ar III] λ7135 emission lines. The *F450W* filter has a bandpass of 3700–5200 Å and covers the [O II] λλ3726, 3729 and [O III] λλ4959, 5007 lines.

All chosen data sets were already processed by the standard *HST* pipeline and optimized by the Hubble Legacy Archive. Each data set included Wide Field Camera (WFC) chip images as well as Planetary Camera (PC) chip images, pieced together to form a single image. The PC chip images were resized to match the WFC scale.

Using the IRAF task *skymap*, the 20 *HST* images were aligned according to their WCS coordinates. *skymap* indicated the shift and rotation required to align each *HST* image relative to each other on a large and empty WCS coordinates map. The alignment of each image was then carefully corrected by comparing the position of stars common to multiple images. The resulting maximum alignment error between each image is about of one pixel, or 0.1 arcsec. Images of same year and filter were pieced together with IDL to create multiple large mosaics of Cas A. Six mosaics were created with this procedure, for each filter and year combination. Before piecing the *HST* images together, the borders of each one were cut, removing bad pixels and CCD seams. In the case where *HST* images would overlap, one image was simply pasted over the other, privileging WFC chip images over PC chip images.

3 RESULTS AND DISCUSSIONS

3.1 Quasi-stationary flocculi

Several slow-moving QSFs have been detected in our data. Fig. 2 shows the position of the QSFs in our field, and Table 3 lists their coordinates, radial velocity and line ratio. Fig. 3 shows the spectra of two QSFs, one 'pure' and the other one on the line of sight to rapidly expanding filaments.

As reported before, their spectra show prominent Hα and [N II] λλ6548, 6583 lines, with a clear nitrogen enhancement. It must be mentioned that no FMKs nor the MEKs were detected, even though they should be present. This absence can be explained by the fact that they are relatively small and faint as revealed by *HST* (Fesen 2001; Fesen et al. 2011), probably too faint to be detected with the Mégantic telescope. Since the discovery of the QSF made by Baade & Minkowski (1954), various measurements of the radial velocities and [N II] λ6583/Hα ratios have been performed but no systemic evaluation for the velocities or the line ratios has ever been made for the majority of them.

3.1.1 Radial velocities

The radial velocity of several QSFs has already been obtained by van den Bergh (1971) and van den Bergh & Kamper (1985). Since our data include some of them and new ones, we compiled a new list of radial velocity for each QSF (Table 3). After a careful subtraction of the adjacent diffuse nebular component, present across the entire field, we determined the radial velocity of the QSFs by fitting a Gaussian profile to the lines, the centroid returned by the Gaussian fit providing the radial velocity when compared with the rest wavelength. The uncertainties on the centroid were determined from equation 4b of Landman, Roussel-Dupré & Tanigawa (1982).

The determination of their radial velocity is delicate since there are actually two different types of QSFs. As proposed by van den Bergh & Kamper (1985), the QSFs appear in two morphologies: (1) elongated head-tail or 'tadpole-like' objects mainly found in the southern regions and (2) more compact clumps found in the north. In our data, each QSF is composed of many pixels and so many spectra. An analysis of the spectra of all QSFs with both morphologies reveals that the velocity from one end to another of some QSFs can vary greatly, depending on their morphology. For the elongated type, the radial velocity tends to vary largely and gradually from head to tail. To the contrary, the more compact clumps show very little variation. Fig. 4 shows three QSFs located in the southern region of Cas A as viewed by *HST*. Two of those belong to the elongated type, and comparing side by side the spectra taken at different locations along the QSF clearly shows the difference in velocity. The elongated type are identified with a dagger symbol in Table 3.

As for the clumpy ones, there is still a velocity spread from one pixel to the next but is far less obvious than the elongated type. To appreciate the velocity dispersion of a given clumpy QSF, we summed all the spectra composing it and measured the FWHM of the [N II] λ6583 line. In most cases, the width of the [N II] lines was

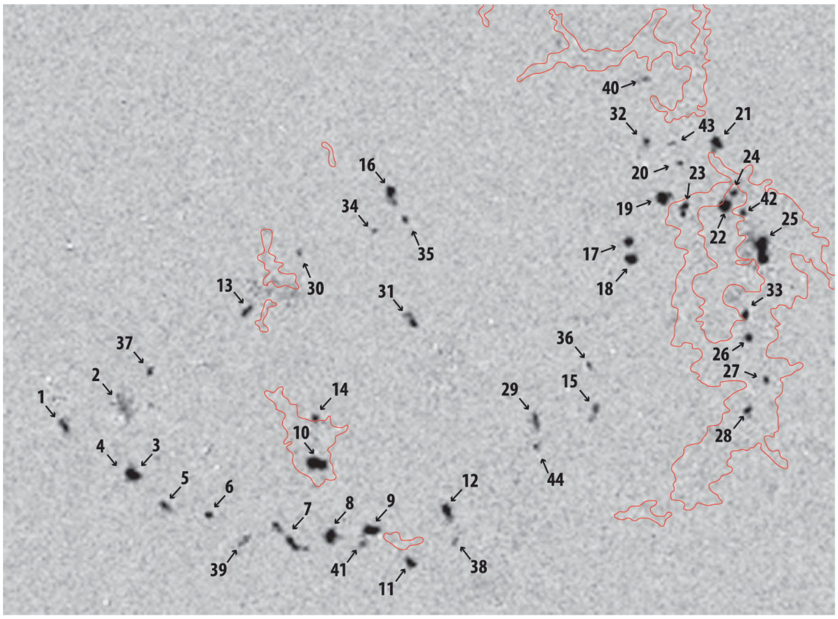

Figure 2. [N II] λ6583 image (5.5 arcmin × 4 arcmin) of Cas A showing the location of the QSFs relative to the main shell observed in [S II] (shown here in red contours). The continuum image, obtained by co-adding the frames of the data cube without emission lines, has been subtracted. Imperfect subtractions in and around bright stars have been manually corrected using the *imedit* task in IRAF. East is to the top, north to the right. To be compared with the Hα image of the same region published by Fesen (2001, fig. 10 in that paper).

larger than that of the diffuse Hα from the ISM surrounding Cas A, which allowed us to estimate the velocity dispersion inside most of the observed QSF. The result is shown in Table 3 under $\Delta V_{\lambda 6583}$.

As pointed out by van den Bergh (1971), most of the radial velocities are negative, ranging from +107 to −579 km s^{-1}. Given the relatively small uncertainties, this indicates a real spread of ∼600 km s^{-1} in the QSF velocity distribution.

Furthermore, we do not measure any significant difference in velocity between Hα and [N II] λ6583 (Table 3). It should be noted that reliable Hα velocities could not be obtained for a large number of clumps due the relative weakness of the line. All radial velocities were corrected for heliocentric and barycentric velocities using the BARYVEL program found in the ASTROLIB[1] package for the IDL programming language.

Fig. 5 shows a comparison between our determination of radial velocities and those compiled by van den Bergh & Kamper (1985), which have been obtained by different sources. Despite the inhomogeneity of the previous data (in terms of instruments, uncertainties in slit locations, absence of error estimates), we note a clear correlation between our data and the others. Measurements by Minkowski in the 1950s are systematically blueshifted by ∼70 km s^{-1}, whereas that of Kirshner & Chevalier (1977) is redshifted by a similar amount. QSF 31 is very peculiar, and although our average velocity is in excellent agreement with that of van den Bergh & Kamper (1985), we clearly see a spatial velocity gradient (see Table 3) indicating that its N-S and E-W components might actually come from two physically distinct substructures. QSF 31 also displays the largest negative velocity of all QSFs (−579 km s^{-1} for component a). Unfortunately, no *HST* images of this region are available.

In order to facilitate comparisons between our data and future observations by others, we have also measured the radial velocity of two diffuse Hα regions found around Cas A, which can be used as references. One is found in the east (23$^{\mathrm{h}}$ 23$^{\mathrm{m}}$ 48$^{\mathrm{s}}$.23 +58° 48′ 30″) for which we measured a radial velocity of −13 ± 10 km s^{-1} and one region in the north-west (23$^{\mathrm{h}}$ 23$^{\mathrm{m}}$ 09$^{\mathrm{s}}$.51 +58° 53′ 53″) with −30 ± 10 km s^{-1}, both corrected for local standard of rest.

[1] http://idlastro.gsfc.nasa.gov/

3.1.2 [N II] λ6583/Hα line ratios

A few *I*(λ6583)/*I*(Hα) ratios have been obtained for some QSFs (van den Bergh 1971; Chevalier & Kirshner 1978; Hurford & Fesen 1996) but no systematic evaluation has ever been conducted. Chevalier & Kirshner (1978) reported that the ratio can range from 1.3 to 5.0 without explicitly listing the ratios for each QSF. Since we detected the great majority of them, it is possible to measure this ratio as long as there is sufficient flux. Unfortunately, some ratios were not measured due to the poor signal-to-noise ratio for both lines. The results are presented in Table 3.

As for the radial velocity, the ratios of [N II] λ6583/Hα were obtained by fitting a Gaussian profile to the lines. We used the peak intensity for both lines returned by the Gaussian fit to evaluate the ratios. The uncertainties on the peak intensity were provided by equation 4a of Landman et al. (1982).

We found that the *I*(λ6583)/*I*(Hα) ratio ranges from 2.3 to nearly 6. The vast majority lies around 3.3 (taking the uncertainties into account) which would indicate that the overabundance of [N II], required to create such a ratio (Chevalier & Kirshner 1978), is more or less the same in all QSFs. We also found that there is no correlation between the position of the QSF and the ratio, suggesting that the nitrogen enhancement in the pre-QSF knots was relatively uniform during the ejection and potentially the same in every direction.

It is interesting to note that the spectra of Cas A's QSFs, as well as the strong nitrogen enhancement they reveal, are very similar to those of the highly clumpy, young Wolf–Rayet nebula M1-67 surrounding the WN8 star WR 124 (Fernández-Martín et al. 2013). Although it is very tempting to suggest that Cas A's QSFs are the densest remains of an older M1-67-like nebula, it is now clear that

Table 3. Positions of the QSFs in Cas A with their radial velocities and [N II]/Hα ratio.

QSF ID	VdB ID[a]	α (2000)[b]	δ (2000)[b]	$V_{r\lambda6548}$ (km s^{-1})	$V_{r\mathrm{H}\alpha}$ (km s^{-1})	$V_{r\lambda6583}$ (km s^{-1})	$\Delta V_{\lambda6583}$ (km s^{-1})	[N II] λ6583/Hα
QSF 1	R40	$23^{h}23^{m}19^{s}.36$	$+58^{\circ}45'51''$	-63 ± 35	-51 ± 17	-54 ± 9	16 ± 30	4.3 ± 1.4
QSF 2		$23^{h}22^{m}43^{s}.80$	$+58^{\circ}46'17''$	-41 ± 24	-53 ± 21	-53 ± 9	0 ± 30	2.7 ± 0.9
QSF 3	R37	$23^{h}23^{m}16^{s}.76$	$+58^{\circ}46'21''$	-55 ± 7	-49 ± 19	-53 ± 2	97 ± 8	3.0 ± 0.2
QSF 4		$23^{h}23^{m}17^{s}.63$	$+58^{\circ}46'14''$			-57 ± 15	0 ± 53	
QSF 5	R38	$23^{h}23^{m}15^{s}.04$	$+58^{\circ}46'34''$	-51 ± 16	-47 ± 19	-48 ± 8	36 ± 26	2.3 ± 0.7
QSF 6		$23^{h}23^{m}14^{s}.60$	$+58^{\circ}46'51''$		-85 ± 31	-109 ± 11	123 ± 37	5.9 ± 1.6
QSF 7a[c]		$23^{h}23^{m}14^{s}.20$	$+58^{\circ}47'17''$			-89 ± 15		3.0 ± 0.8
QSF 7b[c]		$23^{h}23^{m}13^{s}.50$	$+58^{\circ}47'22''$			-25 ± 15		
QSF 7c[c]		$23^{h}23^{m}13^{s}.06$	$+58^{\circ}47'25''$			39 ± 12		
QSF 8a[c]	R20	$23^{h}23^{m}13^{s}.53$	$+58^{\circ}47'38''$			-78 ± 11		3.7 ± 0.3
QSF 8b[c]	R20	$23^{h}23^{m}13^{s}.70$	$+58^{\circ}47'41''$			66 ± 17		
QSF 9a[c]	R21	$23^{h}23^{m}13^{s}.89$	$+58^{\circ}47'54''$			-128 ± 58		3.6 ± 0.3
QSF 9b[c]	R21	$23^{h}23^{m}13^{s}.80$	$+58^{\circ}47'58''$			-81 ± 6		
QSF 10	R9	$23^{h}23^{m}17^{s}.39$	$+58^{\circ}47'38''$	-94 ± 6	-95 ± 6	-93 ± 2	94 ± 6	3.5 ± 0.2
QSF 11	R35	$23^{h}23^{m}12^{s}.21$	$+58^{\circ}48'12''$			11 ± 12	132 ± 42	
QSF 12a[c]	R19	$23^{h}23^{m}15^{s}.06$	$+58^{\circ}48'26''$			-242 ± 14		3.8 ± 0.9
QSF 12b[c]	R19	$23^{h}23^{m}14^{s}.40$	$+58^{\circ}48'28''$			-117 ± 5		
QSF 13	R34	$23^{h}23^{m}25^{s}.16$	$+58^{\circ}47'05''$			-35 ± 10	101 ± 34	
QSF 14	R22	$23^{h}23^{m}19^{s}.76$	$+58^{\circ}47'35''$			-141 ± 10	77 ± 34	
QSF 15		$23^{h}23^{m}20^{s}.17$	$+58^{\circ}49'27''$			70 ± 13	126 ± 46	
QSF 16	R4	$23^{h}23^{m}31^{s}.40$	$+58^{\circ}48'05''$			-193 ± 6	144 ± 19	
QSF 17	R3	$23^{h}23^{m}28^{s}.80$	$+58^{\circ}49'39''$	-93 ± 8	-90 ± 13	-99 ± 3	67 ± 8	3.2 ± 0.3
QSF 18	R2	$23^{h}23^{m}27^{s}.72$	$+58^{\circ}49'41''$	-138 ± 6	-141 ± 12	-137 ± 2	99 ± 8	3.2 ± 0.2
QSF 19	R5	$23^{h}23^{m}31^{s}.17$	$+58^{\circ}49'58''$	-156 ± 11	-166 ± 23	-164 ± 3	140 ± 11	3.4 ± 0.3
QSF 20		$23^{h}23^{m}32^{s}.90$	$+58^{\circ}50'01''$			-167 ± 14	46 ± 48	
QSF 21	R27	$23^{h}23^{m}33^{s}.97$	$+58^{\circ}50'18''$	-10 ± 15	-13 ± 12	-12 ± 5	135 ± 17	3.5 ± 0.4
QSF 22	R7	$23^{h}23^{m}30^{s}.74$	$+58^{\circ}50'19''$	-19 ± 6	-16 ± 6	-18 ± 2	96 ± 6	3.3 ± 0.2
QSF 23		$23^{h}23^{m}30^{s}.52$	$+58^{\circ}50'03''$			-283 ± 10	108 ± 34	
QSF 24	R26	$23^{h}23^{m}31^{s}.38$	$+58^{\circ}50'23''$			-140 ± 18	138 ± 63	
QSF 25	R29	$23^{h}23^{m}28^{s}.36$	$+58^{\circ}50'34''$	-54 ± 13	-53 ± 15	-50 ± 4	147 ± 15	3.3 ± 0.3
QSF 26		$23^{h}23^{m}25^{s}.12$	$+58^{\circ}50'29''$			-253 ± 15	75 ± 51	
QSF 27		$23^{h}23^{m}23^{s}.83$	$+58^{\circ}50'30''$		3 ± 21	-7 ± 7	69 ± 24	3.5 ± 0.7
QSF 28	R11 & R12	$23^{h}23^{m}19^{s}.94$	$+58^{\circ}50'28''$			-161 ± 16	116 ± 56	
QSF 29	R23	$23^{h}23^{m}19^{s}.53$	$+58^{\circ}49'02''$			-175 ± 17	83 ± 59	
QSF 30	R24	$23^{h}23^{m}26^{s}.23$	$+58^{\circ}47'25''$			-32 ± 13	28 ± 44	
QSF 31a[c]	R1	$23^{h}23^{m}24^{s}.75$	$+58^{\circ}48'13''$			-579 ± 27	210 ± 71	
QSF 31b[c]	R1	$23^{h}23^{m}24^{s}.46$	$+58^{\circ}48'26''$			-358 ± 23		
QSF 31c[c]	R1	$23^{h}23^{m}25^{s}.03$	$+58^{\circ}48'11''$			-406 ± 19		
QSF 32	R31	$23^{h}23^{m}13^{s}.30$	$+58^{\circ}48'30''$			-297 ± 23	108 ± 45	
QSF 33	R17	$23^{h}23^{m}25^{s}.88$	$+58^{\circ}50'25''$			-368 ± 24	195 ± 83	
QSF 34	R25	$23^{h}23^{m}28^{s}.31$	$+58^{\circ}47'30''$			-255 ± 31	137 ± 107	
QSF 35		$23^{h}23^{m}30^{s}.00$	$+58^{\circ}48'11''$			-220 ± 58		
QSF 36		$23^{h}23^{m}22^{s}.43$	$+58^{\circ}47'24''$			6 ± 22	142 ± 75	
QSF 37	R34	$23^{h}23^{m}22^{s}.04$	$+58^{\circ}46'27''$			107 ± 13	176 ± 46	
QSF 38	R19	$23^{h}23^{m}13^{s}.09$	$+58^{\circ}48'30''$			-295 ± 21	164 ± 72	
QSF 39		$23^{h}23^{m}13^{s}.26$	$+58^{\circ}47'06''$			-171 ± 37	155 ± 80	
QSF 40	R28	$23^{h}23^{m}37^{s}.11$	$+58^{\circ}49'46''$					
QSF 41		$23^{h}23^{m}13^{s}.65$	$+58^{\circ}47'53''$			-35 ± 28	107 ± 59	
QSF 42		$23^{h}23^{m}30^{s}.30$	$+58^{\circ}50'26''$					
QSF 43	R30	$23^{h}23^{m}33^{s}.95$	$+58^{\circ}49'58''$			-270 ± 26	172 ± 90	
QSF 44		$23^{h}23^{m}18^{s}.15$	$+58^{\circ}49'03''$			-280 ± 18	105 ± 63	

[a]The van den Bergh & Kamper QSF identifications come from van den Bergh & Kamper (1985).
[b]The coordinates were taken directly from the WCS coordinates from the *HST* data archive at CADC. The uncertainty on the position is ± 1 arcsec.
[c]Different velocities along the same QSF as indicated in Fig. 4.

the progenitors of the two objects were very different beasts: a single massive O star, turned into a Wolf–Rayet after a luminous blue variable phase in the case of WR 124 and an $\sim 20\,\mathrm{M}_{\odot}$ binary star in the case of Cas A. However, it is also obvious that CNO-processed material was ejected in a very clumpy wind during a pre-SN phase in both cases.

3.2 Proper motion map of Cas A

A lot of spectroscopy has been conducted for the last half century and multiple radial velocity measurements for several knots (ejecta) were acquired, especially for those located in the bright shell of Cas A. But very few measurements of the proper motion (angular

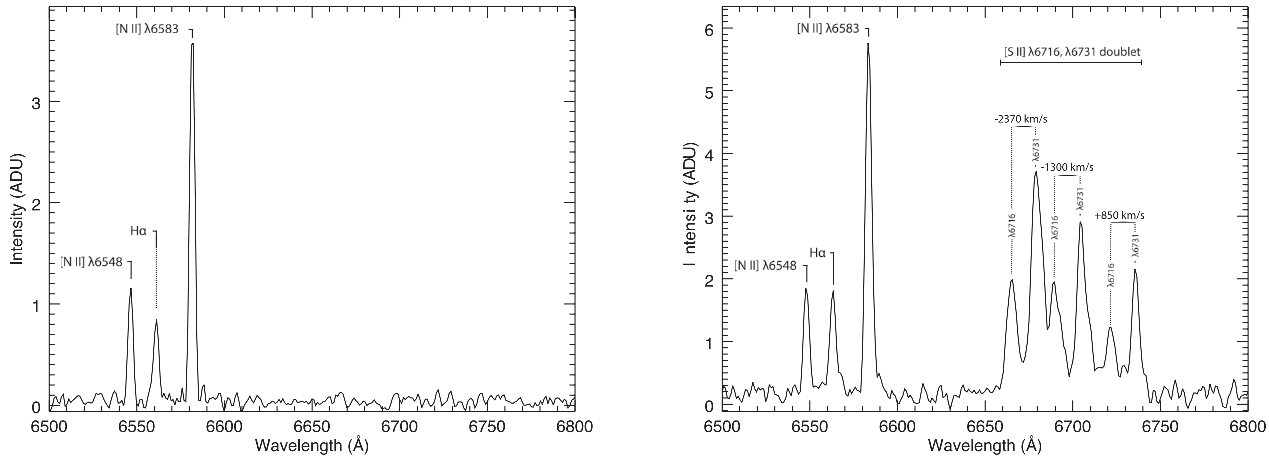

Figure 3. Left: spectrum of QSF 18 showing only Hα and the [N II] λλ6548, 6583 doublet. Right: spectrum of QSF 25 in the line of sight of three [S II] λλ6716, 6731 filaments having different Doppler shifts.

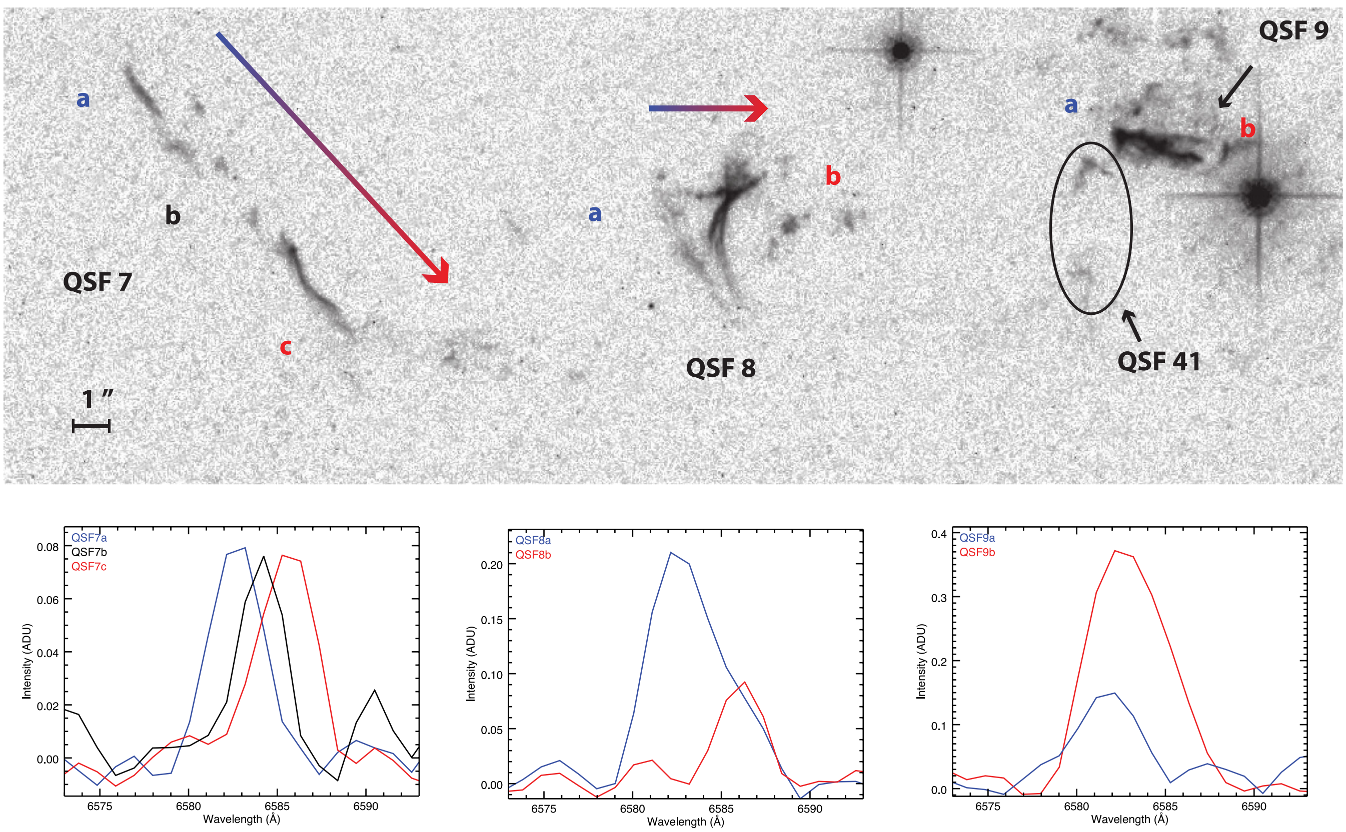

Figure 4. Examples of QSFs with and without elongated structure located in the southern region of Cas A, as seen by *HST*. The radial velocity measured along these QSFs shows gradual change (coloured arrows) for the elongated type (QSF 7 and 8) and only a small change in velocity for clumpy morphology (QSF 9).

displacement) of those knots have been obtained (van den Bergh & Dodd 1970; Kamper & van den Bergh 1976). Using the multi-epoch imaging of Cas A from *HST*, it is possible to look for changes in positions for many knots and estimate their displacement during a given period of time. Doing so, for a maximum of knots, would result in a map showing the angular displacement for various filaments throughout the nebula.

Even though the concept is relatively simple, putting it into practice is not. After all, the filaments of Cas A are in constant evolution, some structures appear and disappear even during short periods of time, as clearly shown by observations (Morse et al. 2004). This undoubtedly makes a precise measurement of the transverse velocity difficult, not to mention the possibility of deceleration of some knots altering the evaluation of their velocity.

Fortunately, the changes that are happening during a short period of time are minimal. When we take a look at two observations separated by a few years, we clearly see some parts emerging and some vanishing but countless details in the morphologies remain the

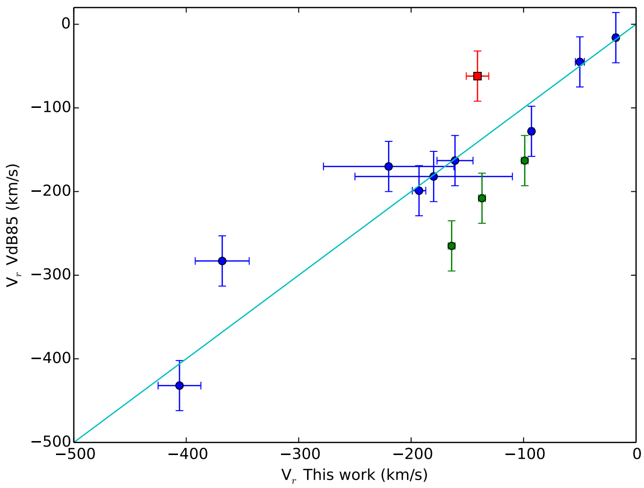

Figure 5. Comparison between our measured values of QSF radial velocities and those compiled by van den Bergh & Kamper (1985) from different sources. A uniform uncertainty of ±30 km s^{-1} was assumed for all data other than ours. Red: Kirshner & Chevalier (1977), green: Minkowski [in the 1950s, compiled by van den Bergh & Kamper (1985)], blue: van den Bergh and collaborators.

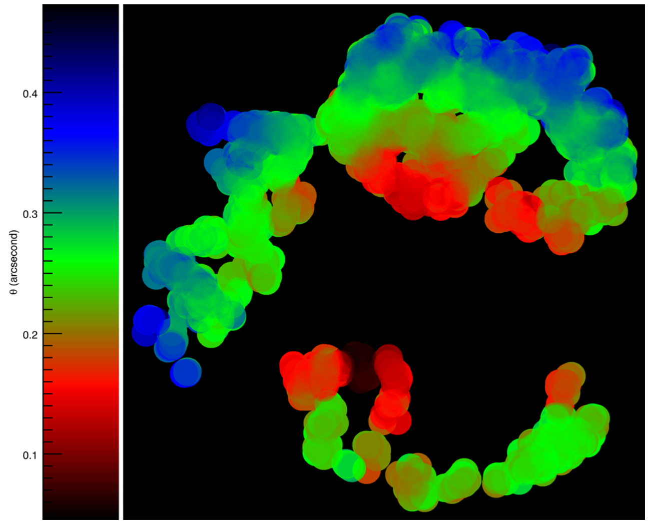

Figure 6. Annual displacement map of Cas A obtained by tracing the displacement of 3500 knots between 2000 and 2008 (see the text).

same. By taking our multi-epoch mosaics, we carefully looked for diverse morphologies and retraced their evolution as they evolved in time. We first retraced the proper motion of several filaments between 2000 and 2002 for both filters independently (*F450W*, *F675W*) and repeated the same procedure for the changes that have taken place between 2002 and 2008. Each displacement was marked and confirmed by eye to make sure that the morphology of a knot has remained the same over time and that it was compact enough to be able to securely identify its centroid. Therefore, by marking each displacement with a vector for each visually confirmed knot, and doing so for all of our mosaics, we were able to create a map containing the positions, directions and displacements of 3500 knots. The map was then rescaled to represent the proper motion per year by averaging the angular displacements for both periods (2000–2002 and 2002–2008).

Since the map is originally made up solely from vectors, we can create a more visually informative map by taking the average of the nearest neighbour around the vectors at a certain radius, allowing us to fill the gap between missing vectors and 'smooth' the angular displacement throughout the surface of Cas A. The result is shown in Fig. 6. As expected for a spherical expansion, the annual angular displacement is lower towards the centre and faster on the outside with a maximum displacement of nearly 0.48 ± 0.1 arcsec yr^{-1}, giving a glimpse of the third dimension of the main shell. Unfortunately, the northern and southern jets are not visible since our multi-epoch mosaic did not cover them.

This map was quite useful as it served to re-estimate the distance to Cas A (Section 3.4) and obtain a three-dimensional spatial view of the remnant (Section 3.5).

3.3 Doppler deconvolution

The hyperspectral cubes obtained are of great interest, especially because they include the emission of the [S II] λλ6716, 6731 lines, allowing the determination of the electron density. Also, it is possible to determine the radial velocity of every line in every spectrum, which can be used to create a three-dimensional view of Cas A. Considering the fact that almost all of the [S II] lines are Doppler shifted, it is quite a daunting task to locate and apply a Gaussian fit manually to every line, especially when about 5000 spectra are available.

For the sake of simplicity, we used an algorithm that allows the identification of the spectral lines by measuring their spectral shifts and their intensities. Our deconvolution technique is very similar to the one developed by Charlebois et al. (2010) based on Čadež, Carramiñana & Vidrih (2004). We identify the emission lines and their common Doppler shifts by defining a Doppler velocity-dependent weight for each line of interest in a spectrum as

$$w_i\,(v) = \int_{-\infty}^{\infty} S\,(\lambda) \exp\left(-\frac{(\lambda - \lambda_i\,(1 + v/c))^2}{2\sigma^2}\right) \mathrm{d}\lambda, \tag{1}$$

where w_i is the probability of finding an emission line with rest wavelength λ_i in a spectrum $S(\lambda)$ at a radial velocity v and σ is the width of the line. It must be mentioned that for most spectra and especially for the cube taken with the second red filter, nearly all of the filaments emit in [S II]; therefore, we define a global probability $\Omega(v)$ of finding an emitting filament at velocity v as follows:

$$\Omega(v) = w_{\lambda 6716}(v) w_{\lambda 6731}(v). \tag{2}$$

The [S II] emission comes as a doublet where both lines are of approximately equal brightness, which allows the use of this deconvolution technique even if there are only two lines. Fig. 7 shows an example of a spectrum being deconvolved applied on the cube taken with the second red filter. The algorithm scans through a given velocity range and estimates the probability of finding an [S II] doublet at a given velocity. The higher the intensity of the doublet, the higher the probability of finding that doublet at a certain velocity. The velocity is then given by the peak intensity in the $\Omega(v)$ profile. If more than one doublet is in a spectrum, then multiple peaks will arise in the $\Omega(v)$ profile, giving multiple possible velocities. After the scan is completed, each doublet is identified in the spectrum according to the velocity found earlier. Once a doublet is confirmed with a given velocity, each line is then fitted with a Gaussian profile. The centroid returned by the fit allows a more accurate determination of the velocity. This procedure is applied to every spectrum of each and every pixel found in a hyperspectral cube. While performing the deconvolution, we can replace the wavelength axis by the radial velocity while conserving the spatial dimension to create a 3D

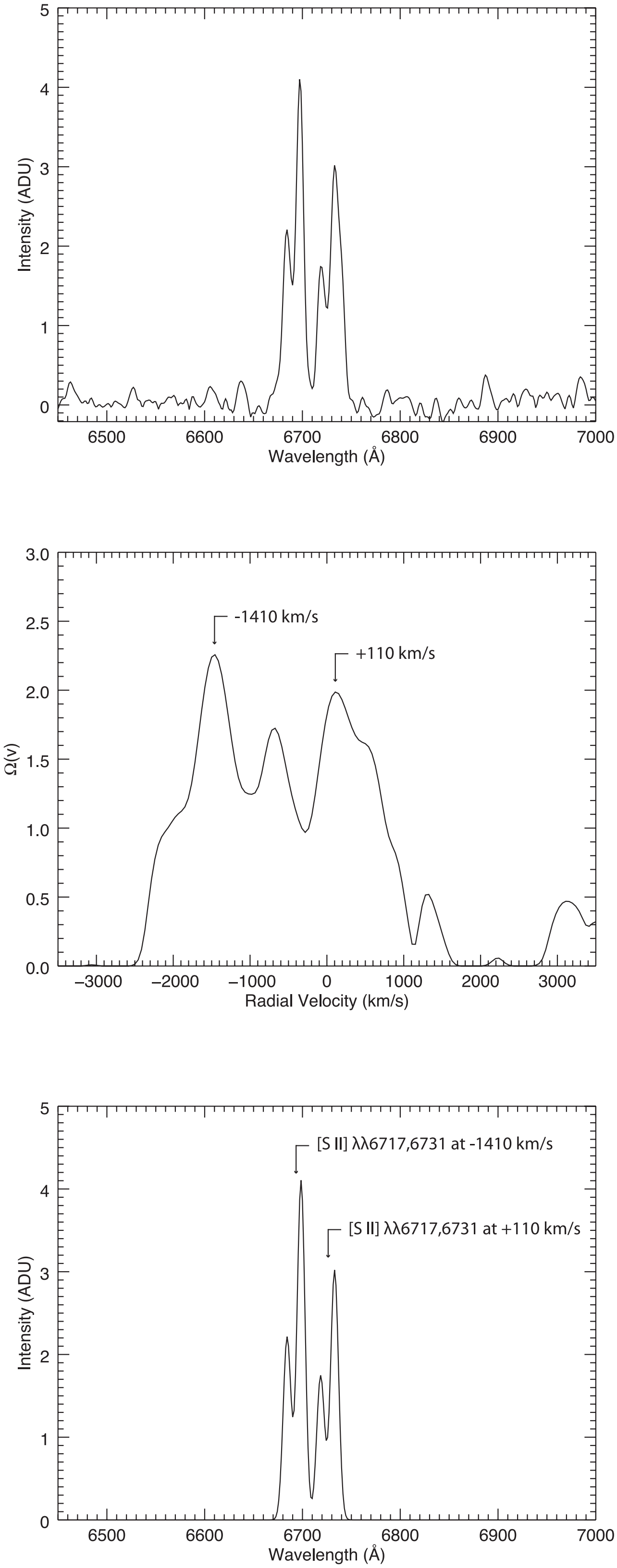

Figure 7. Upper panel: example of a single spectrum extracted from the second red data cube of Cas A. Middle panel: the combined probability $\Omega(v)$ of finding the doublet [S II] λλ6716, 6731 at a given velocity. Lower panel: deconvolved spectrum showing the velocity for each [S II] doublet.

velocity map. Combining this map with the angular displacement map (Section 3.2), we obtain a full three-dimensional spatial view of Cas A, the method and results being discussed in Section 3.5.

3.4 Distance to Cas A – revisited

The distance to Cas A has been estimated many times using several observations and techniques (Minkowski 1959; van den Bergh 1971; Sakhibov 1980; Braun 1987; Reed et al. 1995). The latest estimate comes from Reed et al. (1995) who used three methods to derive multiple distances to Cas A (see table 3 of Reed et al. 1995). One method was developed by Braun (1987) which makes use of both the radial velocity and the proper motion. Using a large sample of radial velocities and multiple values for the proper motion, he estimated that Cas A must lie between 2.9 and 3.9 kpc. The main uncertainty in the calculation comes from the derivation of the averaged proper motion which needed a centre of explosion that happened at a given time. Many possible centres were calculated from observations at different wavelengths, and the date of the explosion is still uncertain and possibly occurred between the derived date of 1657 by Kamper & van den Bergh (1976) and the Flamsteed date of 1680. This leads to multiple estimates of a distance, and Reed et al. (1995) favoured $3.4^{+0.3}_{-0.1}$ kpc by averaging all of his derived distances.

Our multi-epoch mosaic of Cas A taken with *HST* allows us to create a map showing the angular displacements of various knots. Combining both the radial velocity (see Section 3.3) and the angular displacement maps, it is possible to derive a distance to Cas A without the need of a centre or a date of the explosion.

The expansion velocity of an isotropically expanding shell can be expressed as

$$V_{\rm exp}^2 = V_{\rm r}^2 + V_{\rm t}^2, \tag{3}$$

where $V_{\rm r}$ and $V_{\rm t}$ are the radial and transverse velocities, respectively. The transverse velocity can be obtained with

$$V_{\rm t} = D\theta/t, \tag{4}$$

where D is the distance to the object and θ the angular displacement that occurs during a given period of time t. Hence, we can estimate the distance to Cas A using

$$V_{\rm exp}^2 = V_{\rm r}^2 + (D\theta/t)^2, \tag{5}$$

when the expansion velocity $V_{\rm exp}$ is known.

This relation is valid only in the case of a uniformly expanding shell. However, it is obvious that Cas A is not expanding perfectly uniformly due to a turbulent and asymmetric explosion as suggested by both observations and simulations. The detection of high-velocity, sulphur-rich ejecta along the remnant's north-east and south-west limbs suggests an asymmetric expansion, possibly even bipolar (Fesen 2001). The asymmetry was also detected in the SN photosphere based on the light echo spectra that indicate that Cas A was an intrinsically asymmetric SN (Rest et al. 2011). Additionally, SN explosion models predict substantial asymmetries due to instabilities prior to the explosion (Blondin, Mezzacappa & DeMarino 2003; Burrows et al. 2007; Hammer, Janka & Müller 2010).

Despite the obvious asymmetry in the explosion and the resulting velocity spread of the knots, previous studies have demonstrated that the ejecta knots lie roughly on a spherical shell, which travelled radially outwards from a unique centre of explosion (Lawrence et al. 1995; Reed et al. 1995; DeLaney et al. 2010; Milisavljevic & Fesen 2013). Knowing that the knots' velocities can be fitted by a spherical expansion model and being aware of the existence of the velocity spread, we can still use the last relation to estimate the distance.

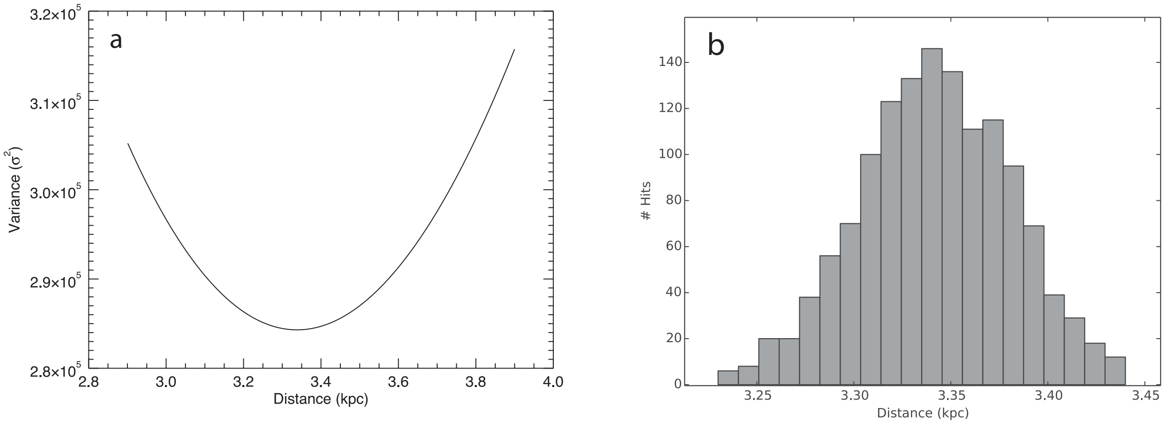

Figure 8. (a) Variance for multiple expansion velocity distributions as a function of the distance to Cas A. The location on the curve where the variance is minimal corresponds to a distance of 3.33 kpc. (b) Results of multiple distance estimates taking into account the uncertainties on the radial and transverse velocity maps (see the text for more details).

In a case of a perfectly spherical shape, all ejecta would have exactly the same velocity. But since there is a spread in the velocity distribution, and we know that the shape of the shell is somewhat close to spherical, one can look for a distance where the distribution of the expansion velocity is minimal, which is the same as minimizing the velocity distribution around a spherical shell. By varying the distance from 2.9 to 3.9 kpc, we look for a distance where the variance of the distribution is the lowest, with the variance being expressed as

$$\sigma^2 = \frac{\sum_{i=0}^{n} \left(v_{\mathrm{exp}_i} - \overline{v_{\mathrm{exp}}}\right)^2}{N}, \tag{6}$$

where N is the number of knots used for the evaluation. The variance for multiple expansion velocity distributions as a function of assumed distances of Cas A has been determined, and the result is shown in Fig. 8(a). As expected, as we approach the 'right' distance, the variance of the velocities distribution diminishes until we pass a certain point where the variance starts to increase. The originality of this method is that we do not need to adjust anything; instead we look for a distance where the dispersion of the distribution of the expansion velocities is minimal, the only criterion being that the object needs to be somewhat close to spherical symmetry.

The minimum on the curve indicates the distance at which the dispersion of the velocity distribution for all knots is minimal, corresponding to a distance of 3.33 ± 0.10 kpc. The uncertainty was found by taking into account the uncertainties on the radial and transverse velocity maps. Despite considerable care in measuring the proper motion, some knots might have an error as large as $\pm$ 0.2 arcsec (or 3223 km s^{-1} at 3.4 kpc), which could greatly affect the distance estimate. Also, the deconvolution used to estimate the radial velocity has uncertainties of about $\pm$50 km s^{-1}.

To explore the impact of such large errors on the distance estimate, we wrote a simple algorithm that redraws the maps by varying the value by the uncertainties for every point in either map randomly. Then, using the redrawn maps, we re-estimate the distance using the variance. For each new map, we obtained a new curve just like Fig. 8(a) but measured a new minimum so a new distance. By drawing at least a thousand maps, we can have an idea of how the uncertainties affect the distance estimate and gave lower and upper values for possible distances. The results are shown in Fig. 8(b). We found that the distances derived were always above 3.23 kpc and below 3.44 kpc no matter how many maps can be drawn. Therefore, we assume a distance of 3.33 with an uncertainty of 0.10 kpc.

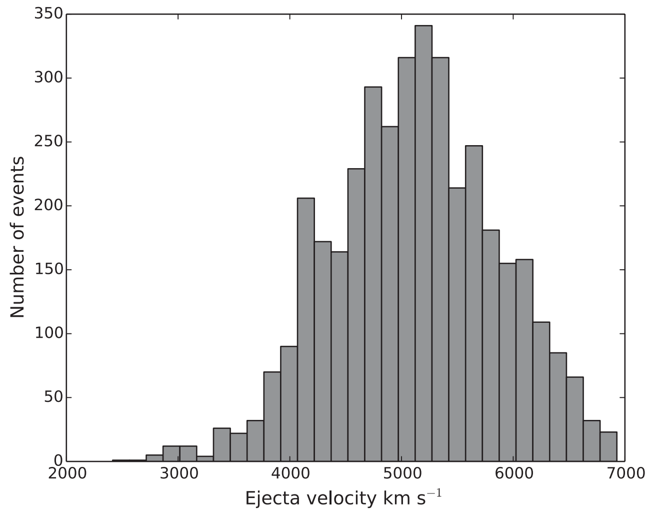

Figure 9. Distribution of the knot space velocity obtained by combining both the radial and transverse velocity maps assuming a distance of 3.33 kpc.

With fewer assumptions, we found that our derived distance is in very good agreement with the one found earlier by Reed et al. (1995). Using our distance, it is possible to evaluate the space velocities of the knots and obtain a histogram that shows the distribution of the ejecta velocity within the bright shell (Fig. 9). From that histogram, it is clear that there was an asymmetry in the explosion that propelled several knots with different velocities. We found that most of the ejecta velocities lie between 4000 and 6000 km s^{-1} (80 per cent) and nearly half between 4500 and 5500 km s^{-1} (49 per cent). Because it is even more informative to visualize the position of the knots in the bright shell, we have created the 3D spatial view of Cas A discussed in the next section.

3.5 Three-dimensional spatial view of the remnant

Milisavljevic & Fesen (2013) recently obtained an impressive three-dimensional spatial view of Cas A based on radial velocity measurements extracted from long-slit and multi-slit spectra. The data were collected during three years, and an extensive 3D Doppler reconstruction was undertaken in other to obtain a 3D spatial view of

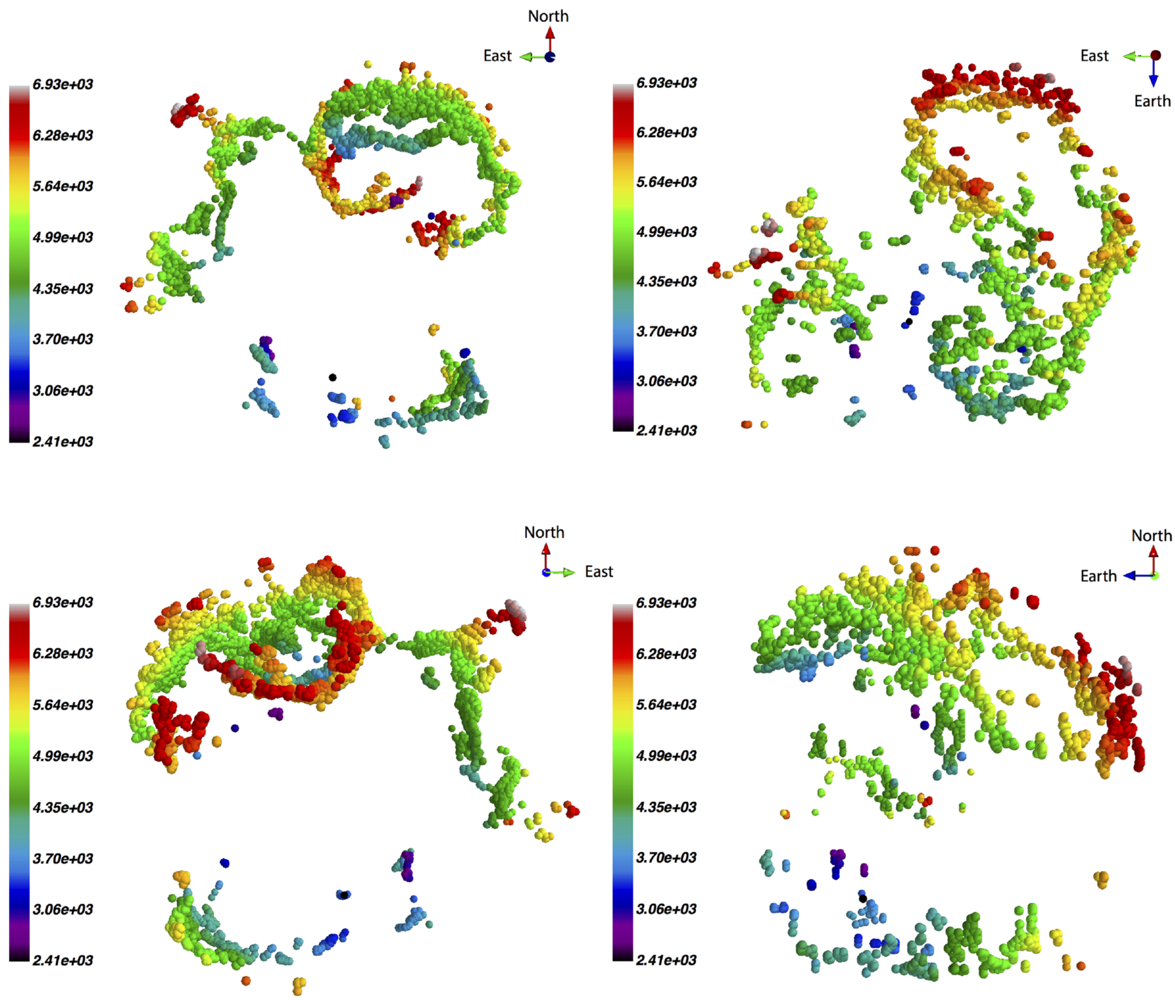

Figure 10. Three-dimensional spatial view of Cas A. The colour bar indicates the knots velocity. Upper right: Cas A as viewed from Earth. Upper left: viewed from top. Lower left: viewed from the back. Lower right: viewed from the side. Refer to Movie 1 for an animation of these data (available in the online journal).

the remnant. Since we also have enough information to reconstitute the 3D appearance of the main shell, we want to introduce a technique far different and simpler than the one used by Milisavljevic & Fesen (2013).

In Section 3.4, we used the radial and transverse velocities to obtain an estimate of the distance to Cas A. With this estimate in hand, we can re-evaluate for each knot the transverse velocity with its corresponding radial velocity to determine a three-dimensional spatial view of the remnant. For every knot, we simply have to combine both velocities using the Pythagorean relation to obtain the global velocity and at the same time determine the direction in which it is travelling. Then, using a simple three-dimensional Cartesian plane, the centre representing the location of the explosion, we can determine the distance travelled by each knot since the explosion (325 years ago; Fesen et al. 2006b) assuming that no deceleration has occurred since that time. Once the location is found, we mark the position by a point in the Cartesian grid and associate it with a colour indicating its current velocity. The result is shown in Fig. 10. This method differs from that employed by DeLaney et al. (2010) and Milisavljevic & Fesen (2013), who use a scaling factor to convert projected radii from the centre of explosion to projected velocities. The scaling factor being found by fitting the measured Doppler velocities to a spherical expansion model.

Fig. 10 allows us to distinguish the expansion velocity of various filaments throughout the remnant from different perspectives. This figure should be compared with fig. 6 of Milisavljevic & Fesen (2013), the main difference being in the way the velocity is presented in colour coding. Fig. 10 shows the space velocity of the filaments whereas Milisavljevic & Fesen (2013) express it in terms of radial velocity. Also, we have not used any surface reconstruction in order to smooth the point cloud, which explains why our view seems thinner compared to Milisavljevic & Fesen (2013). It should be noted that the view of Milisavljevic & Fesen (2013) is more complete, since they cover in more detail the ejecta and also show the high-velocity outer material.

From Fig. 10, it is clear that the main shell ejecta are not distributed homogeneously in space but rather in arc- and ring-like structures as clearly shown by Milisavljevic & Fesen (2013). There is also a clear velocity asymmetry, first recognized by Minkowski (1968) and later clearly shown by Lawrence et al. (1995) and Reed et al. (1995). The expansion velocity varies greatly from the front to the back of the remnant. We measured space velocities of about 5000 km s^{-1} for the ejecta travelling in our direction and an expansion of nearly 7000 km s^{-1} for those that are moving away from us (lower right of Fig. 10). Although the geometry is close to spherical, our view shows a slight elongation along the line of sight. This is a clear indication that some deceleration had occurred in front of the remnant and as Reed et al. (1995) mentioned, it seems that the circumstellar medium's density around Cas A gradually varies from the front to the back, with the front having a much higher density that has slowed down the expansion considerably. In the back, the circumstellar density surrounding the remnant seems a little more complex. When we look at the remnant from the top, we can see a clear cut in the distribution of the ejecta (upper right of Fig. 10) also observed by Milisavljevic & Fesen (2013). From that perspective, we see no ejecta to the east while in the west we found several with relatively high velocity. It is as if the ejecta are moving through a cavity with much lower density than in the east.

3.6 Electron density

The electron density can be obtained from the [S II]λ6716/[S II]λ6731 line ratio when the temperature is known. Published values for this ratio indicate variations ranging from 0.4 to 1.7 at different locations in Cas A (Peimbert & van den Bergh 1971; Kirshner & Chevalier 1977; Reed et al. 1995). This clearly shows a great variation in the electronic density in the remnant. Surprisingly, no systematic investigation of how this ratio varies throughout the nebula has ever been conducted. Using our data, we were able to determine this ratio at many locations in the remnant. To better visualize the result, we created a second three-dimensional spatial view of the remnant showing the variation of the doublet ratio throughout the vast majority of the remnant. The result is shown in Fig. 11, where the colour scale represents the [S II]λ6716/[S II]λ6731 ratio. For the sake of clarity, we focus on two regions, as indicated by the arrows in the upper panel of Fig. 11.

We only used lines with a signal-to-noise ratio greater than 6 to make sure that we do not overestimate the [S II] λ6716/[S II] λ6731 ratio, as suggested by Rola & Pelat (1994). We also kept only ratio with an uncertainty of about ±0.1. Such a rigorous threshold leads to the rejection of many spectra even if the doublet is clearly visible in the data. Nonetheless, there are a sufficient number of spectra available after the selection to show that the ratio greatly varies from one region to the next. A histogram of the [S II] doublet ratio (Fig. 12) shows that most of the ratios lie between 0.39 and 1.1 with very few knots having a ratio higher than 1.1. Figs 11(b) and (c) also show that the ratio can vary quite dramatically from one region to another without any gradient linking them with some approaching both the low and high density, $n_e \leq 10^2$ cm^{-3} and $n_e \geq 10^4$ cm^{-3}, respectively (atomic data from Osterbrook & Ferland 2006). But most of the knots have an electronic density between $10^3\ T_4$ cm^{-3} and $10^4\ T_4$ cm^{-3}, where $T_4 = (10^4/T)^{1/2}$. With the vast majority of the ratio around 0.5, this undoubtedly indicates that the electronic density (and therefore the density of the ejecta) is very high, as expected. With these data, we could not confirm the marginal trend in the [S II] ratio between the front and back reported by Reed et al. (1995).

4 SUMMARY

We used the imaging Fourier transform spectrometer SpIOMM to obtain hyperspectral cubes of Cas A SNR. Each cube contains over 5000 spatially resolved spectra covering the spectral range 6480–7050 Å. We also used multi-epoch observations from *HST* acquired with the broad-band *F675W* and *F450W* filters between 2000 and 2008. Specific results and conclusions coming from each instrument and a combination of both are as follows.

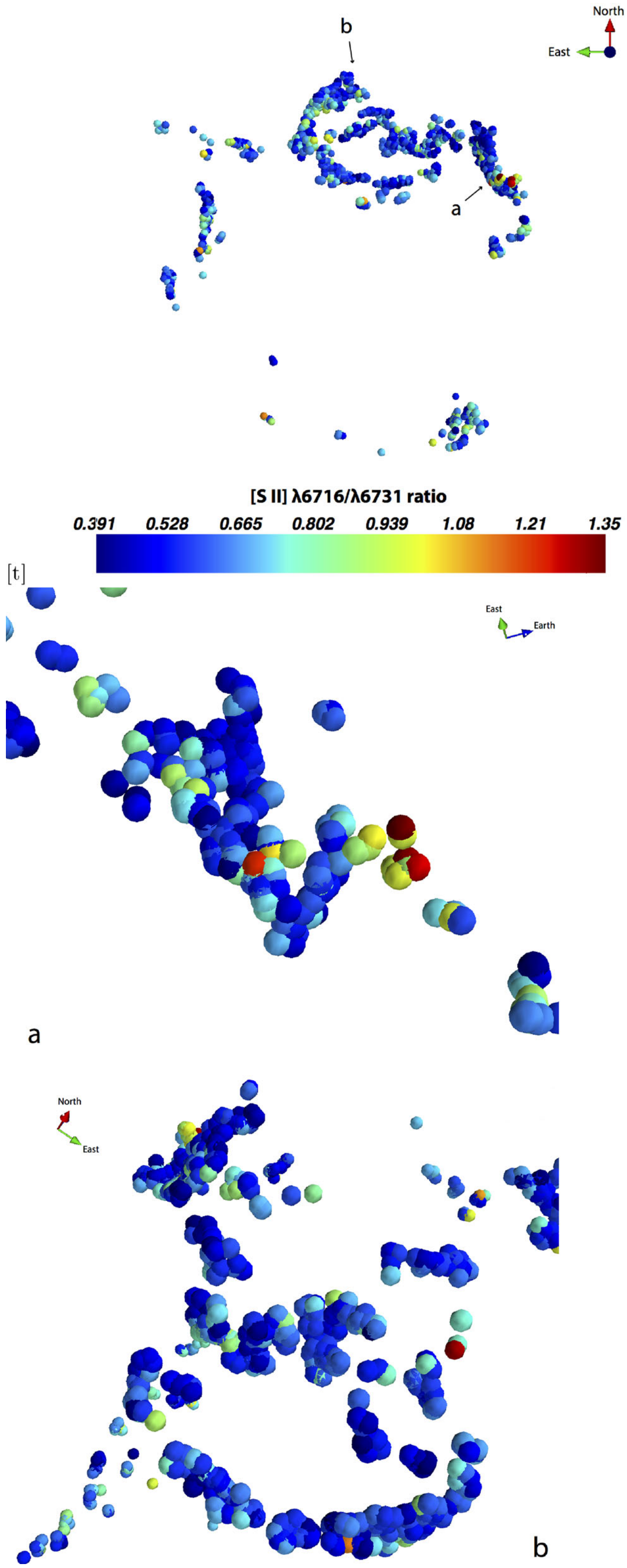

Figure 11. Ratio of the [S II] λ6716/[S II] λ6731 line for various locations in the remnant as represented by the colour bar. Upper image: as viewed from the Earth. Middle images: viewed from inside as indicated by the arrow a. Lower image: viewed from behind as indicated by the arrow b. Refer to Movie 2 for an animation of these data (available in the online journal).

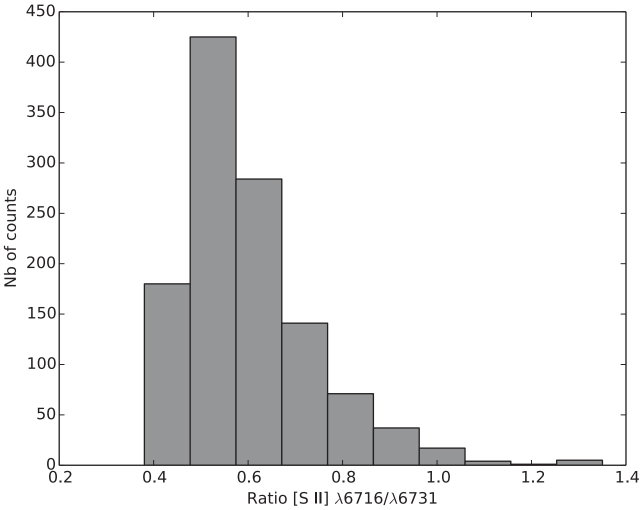

Figure 12. Histogram of the [S II] λ6716/[S II] λ6731 line ratio.

(1) From SpIOMM observations, we identified the N-rich clumps QSFs and measured their radial velocity and [N II] λ6583/Hα ratio. We found that the [N II] λ6583/Hα ratio varies little from one QSF to another, with an average of 3.5 ± 0.5. We saw no correlation between the radial velocity, the [N II] λ6583/Hα ratio and the position of the QSF in the remnant.

(2) From *Hubble* observations, we created mosaics in order to measure the proper motion of 3500 knots. From these measurements, we created a proper motion map that clearly shows the displacement of several filaments throughout the vast majority of the remnant. This map provides a glimpse of the third dimension by showing a gradient in velocity from the centre to the edge of the remnant. The proper motion measured varied from 1700 to 6800 km s^{-1} assuming a distance of 3.33 kpc.

(3) Combining the 3D velocity map obtained from SpIOMM and the proper motion map from *Hubble*, we have re-evaluated the distance to Cas A with the only assumption that Cas A should be close to spherical. We looked for a distance by minimizing the variance in the distribution of the expansion velocity. By scanning through reasonable values of the distance to Cas A, we estimate a most likely value to be 3.33 ± 0.10 kpc, consistent with previous estimates.

(4) With the distance directly derived from our data, we then estimate from our proper motion map the transverse velocity. Combining the transverse and radial velocities of the filaments, we created a 3D spatial view of Cas A showing the location, expansion velocity and the [S II] λ6716/[S II] λ6731 line ratio for multiple locations in the remnant. We noticed that the ejecta is far from being uniform around a given centre. We confirm the observations of previous kinematic studies of Cas A, that the ejecta form some arc- and ring-like structures with expansion velocities ranging from 2500 km s^{-1} to nearly 7000 km s^{-1}. The fastest ejecta, belonging to the main shell, are concentrated in the back of the remnant (as viewed from Earth) and also along the base of the northern jet. As for the [S II] ratio, we found in average a relatively low value of 0.5 ± 0.2, indicating a relatively high electronic density, as expected, as well as significant variations across the remnant.

ACKNOWLEDGEMENTS

LD is grateful to the Canada Research Chair programme, the Natural Sciences and Engineering Research Council of Canada, the Fonds de Recherche du Québec-Nature et Technologies (FRQ-NT), as well as the Ministère de l'Enseignement supérieur, de la Recherche, de la Science et de la Technologie (Québec – PCUC program) for financial support. Bernard Malenfant and Ghislain Turcotte, who provided technical help at the telescope, are also gratefully acknowledged. We also thank the referee for constructive remarks that improved the content of this paper.

REFERENCES

Baade W., Minkowski R., 1954, ApJ, 119, 206
Bernier A.-P., Charlebois M., Drissen L., Grandmont F., 2008, Proc. SPIE, 7014, 245
Besel M.-A., Krause O., 2012, A&A, 541, L3
Blondin J. M., Mezzacappa A., DeMarino C., 2003, ApJ, 584, 971
Braun R., 1987, A&A, 271, 233
Burrows A., Dessart L., Ott C. D., Livne E., 2007, Phys. Rep., 442, 23
Charlebois M., Drissen L., Bernier A.-P., Grandmont F., Binette L., 2010, ApJ, 139, 2083
Chevalier R. A., Kirshner R. P., 1978, ApJ, 219, 931
DeLaney T. et al., 2010, ApJ, 725, 2038
Douvion T., Lagage P. O., Cesarsky C. J., 1999, A&A, 352, L111
Drissen L., Bernier A.-P., Charlebois M., Brière É., 2008, Proc. SPIE, 7014, 246
Drissen L. et al., 2012, Proc. SPIE, 8446, 84463S
Ennis J. A., Rudnick L., Reach W. T., Smith J. D., Rho J., DeLaney T., Gomez H., Kozasa T., 2006, ApJ, 652, 376
Fernández-Martín A., Vílchez J. M., Pérez-Montero E., Candian A., Sánchez S. F., Martín-Gordón D., Riera A., 2013, A&A, 554, 104
Fesen R., 2001, ApJS, 133, 161
Fesen R., Morse J. A., Chevalier R. A., Borkowski K. J., Gerardy C. L., Lawrence S. S., van den Bergh S., 2001, ApJ, 122, 2644
Fesen R. A. et al., 2006a, ApJ, 636, 859
Fesen R. A. et al., 2006b, ApJ, 645, 283
Fesen R., Zastrow J. A., Hammell M. C., Shull J. M., Silva D. W., 2011, ApJ, 736, 109
Gotthelf E. V., Koralesky B., Rudnick L., Jones T. W., Hwang U., Petre R., 2001, ApJL, 552, L39
Hammell M. C., Fesen R. A., 2008, ApJS, 179, 195
Hammer N. J., Janka H.-Th., Müller E., 2010, ApJ, 714, 1371
Hughes J. P., Rakowski C. E., Burrows D. N., Slane P. O., 2000, ApJ, 528, L109
Hurford A. P., Fesen R. A., 1996, ApJ, 469, 246
Hwang U., Laming J. M., 2003, ApJ, 597, 362
Isensee K., Rudnick L., DeLaney T., Smith J. D., Rho J., Reach W. T., Kozasa T., Gomez H., 2010, ApJ, 725, 2059
Isensee K. et al., 2012, ApJ, 757, 126
Kamper K., van den Bergh S., 1976, ApJS, 32, 351
Kirshner R. P., Chevalier R. A., 1977, ApJ, 218, 142
Krause O., Birkmann S. M., Usuda T., Hattori T., Goto M., Rieke G. H., Misselt K. A., 2008, Science, 320, 1195
Laming J. M., Hwang U., 2003, ApJ, 597, 347
Landman D. A., Roussel-Dupré R., Tanigawa G., 1982, ApJ, 261, 732
Lawrence S. S., MacAlpine G. M., Uomoto A., Woodgate B. E., Brown L. W., Oliversen R. J., Lowenthal J. D., Liu C., 1995, AJ, 109, 2635
Martin T., Drissen L., Joncas G., 2012, Proc. SPIE, 8451, 84513K
Milisavljevic D., Fesen R. A., 2013, ApJ, 772, 134
Minkowski R., 1959, in Bracewell R. N., ed., Proc. IAU Symp. 9, Paris Symposium on Radio Astronomy. Stanford Univ. Press, Stanford, CA, p. 315
Minkowski R., 1968, Nebulae and Interstellar Matter. University of Chicago Press, Chicago, IL, p. 623
Morse J. A., Fesen R., Chevalier R. A., Borkowski K. J., Gerardy C. L., Lawrence S. S., van den Bergh S., 2004, ApJ, 614, 727

Osterbrook D. E., Ferland G. J., 2006, Astrophysics of Gaseous Nebulae and Active Galactic Nuclei. University Science Books, Mill Valley, CA
Peimbert M., van den Bergh S., 1971, ApJ, 167, 223
Reed J. E., Hester J. J., Fabian A. C., Winkler P. F., 1995, ApJ, 440, 706
Rest A. et al., 2008, ApJ, 681, L81
Rest A. et al., 2011, ApJ, 732, 3
Rola C., Pelat D., 1994, A&A, 287, 676
Sakhibov F. K., 1980, Sov. Astron. Lett., 6, 56
Tananbaum H., 1999, IAU Circ., 7246
Thorstensen J. R., Fesen R. A., van den Bergh S., 2001, AJ, 122, 297
van den Bergh S., 1971, ApJ, 165, 457
van den Bergh S., Dodd W. W., 1970, ApJ, 162, 485
van den Bergh S., Kamper K. W., 1983, ApJ, 268, 129
van den Bergh S., Kamper K., 1985, ApJ, 293, 537
Willingale R., Bleeker J. A. M., van der Heyden K. J., Kaastra J. S., Vink J., 2002, A&A, 381, 1039
Young P. A. et al., 2006, ApJ, 640, 891
Čadež A., Carramiñana A., Vidrih S., 2004, ApJ, 609, 797

SUPPORTING INFORMATION

Additional Supporting Information may be found in the online version of this article:

Movie 1. Movie-1.mov
Movie 2. Movie-2.mov
(http://mnras.oxfordjournals.org/lookup/suppl/doi:10.1093/mnras/stu774/-/DC1).

Please note: Oxford University Press are not responsible for the content or functionality of any supporting materials supplied by the authors. Any queries (other than missing material) should be directed to the corresponding author for the article.

This paper has been typeset from a TEX/LATEX file prepared by the author.